

Combining machine learning algorithms with traditional methods for resolving the atomic-scale dynamic structure of monolayer MoS_2 in high-resolution transmission electron microscopy

Yu Meng(蒙宇), Shuya Wang(王淑雅), Xibiao Ren(任锡标), Han Xue(薛涵), Xuejun Yue(岳学军), Chuanhong Jin(金传洪), Shanggang Lin(林上港), and Fang Lin(林芳)

Citation: Chin. Phys. B, 2025, 34 (**1**): 016802. DOI: 10.1088/1674-1056/ad9ba3

What follows is a list of articles you may be interested in

Multidimensional images and aberrations in STEM

Eric R. Hoglund and Andrew R. Lupini

Chin. Phys. B, 2024, 33 (**9**): 096807. DOI: 10.1088/1674-1056/ad73b2

Revealing the microstructures of metal halide perovskite thin films via advanced transmission electron microscopy

Yeming Xian(冼业铭), Xiaoming Wang(王晓明), and Yanfa Yan(鄢炎发)

Chin. Phys. B, 2024, 33 (**9**): 096803. DOI: 10.1088/1674-1056/ad6259

Cryo-EM combined with image deconvolution to determine ZIF-8 crystal structure

Kang Wu(吴抗), Baisong Yang(杨柏松), Wenhua Xue(薛文华), Dapeng Sun(孙大鹏), Binghui Ge(葛炳辉), and Yumei Wang(王玉梅)

Chin. Phys. B, 2024, 33 (**7**): 076802. DOI: 10.1088/1674-1056/ad48f8

Controllable fabrication of self-organized nano-multilayers in copper-carbon films

Wei-Qi Wang(王伟奇), Li Ji(吉利), Hong-Xuan Li(李红轩), Xiao-Hong Liu(刘晓红), Hui-Di Zhou(周惠娣), Jian-Min Chen(陈建敏)

Chin. Phys. B, 2019, 28 (**3**): 036802. DOI: 10.1088/1674-1056/28/3/036802

Quantitative HRTEM and its application in the study of oxide materials

Chun-Lin Jia(贾春林), Shao-Bo Mi(米少波), Lei Jin(金磊)

Chin. Phys. B, 2018, 27 (**5**): 056803. DOI: 10.1088/1674-1056/27/5/056803

RAPID COMMUNICATION

Combining machine learning algorithms with traditional methods for resolving the atomic-scale dynamic structure of monolayer MoS_2 in high-resolution transmission electron microscopy

Yu Meng(蒙宇)[1,†], Shuya Wang(王淑雅)[1,†], Xibiao Ren(任锡标)[2], Han Xue(薛涵)[3], Xuejun Yue(岳学军)[1], Chuanhong Jin(金传洪)[2,‡], Shanggang Lin(林上港)[1,§], and Fang Lin(林芳)[1,¶]

[1] *Department of Applied Physics, College of Electronic Engineering, South China Agricultural University, Guangzhou* 510642, *China*
[2] *State Key Laboratory of Silicon and Advanced Semiconductor Materials, School of Materials Science and Engineering, Zhejiang University, Hangzhou* 310027, *China*
[3] *Materials Sciences Division, Lawrence Berkeley National Laboratory, Berkeley, CA* 94720, *USA*

(Received 1 October 2024; revised manuscript received 1 November 2024; accepted manuscript online 9 December 2024)

High-resolution transmission electron microscopy (HRTEM) promises rapid atomic-scale dynamic structure imaging. Yet, the precision limitations of aberration parameters and the challenge of eliminating aberrations in *Cs*-corrected transmission electron microscopy constrain resolution. A machine learning algorithm is developed to determine the aberration parameters with higher precision from small, lattice-periodic crystal images. The proposed algorithm is then validated with simulated HRTEM images of graphene and applied to the experimental images of a molybdenum disulfide (MoS_2) monolayer with 25 variables (14 aberrations) resolved in wide ranges. Using these measured parameters, the phases of the exit-wave functions are reconstructed for each image in a focal series of MoS_2 monolayers. The images were acquired due to the unexpected movement of the specimen holder. Four-dimensional data extraction reveals time-varying atomic structures and ripple. In particular, the atomic evolution of the sulfur-vacancy point and line defects, as well as the edge structure near the amorphous, is visualized as the resolution has been improved from about 1.75 Å to 0.9 Å. This method can help salvage important transmission electron microscope images and is beneficial for the images obtained from electron microscopes with average stability.

Keywords: aberration measurement, high-resolution transmission electron microscopy, feature-extraction networks, exit-wave reconstruction, monolayer MoS_2

PACS: 68.37.Og, 43.60.Lq, 43.60.Tj, 81.07.–b, 42.15.Fr

DOI: 10.1088/1674-1056/ad9ba3 **CSTR:** 32038.14.CPB.ad9ba3

1. Introduction

Monolayer materials, e.g., graphene and transition metal dichalcogenides (TMDs), exhibit exceptional physical properties, including unique electrical, optical, magnetic, and catalytic characteristics.[1,2] These properties are influenced by defects and interfaces, which can be precisely engineered.[3] The exotic properties found in various boundary structures of monolayer materials hold great potential for developing new functional and quantum devices in advanced electronic circuits. This expands their applications in electronics, optoelectronics, magnetism, and catalysis.[4,5]

The atomic structure of monolayer materials is typically analyzed using transmission electron microscopy (TEM), including scanning transmission electron microscopy (STEM) and high-resolution transmission electron microscopy (HRTEM). A majority of researchers favor STEM due to its high resolution, which directly reveals atomic structures.[5–8] Compared with STEM, HRTEM offers two key advantages: sensitivity to focus and high-speed imaging. HRTEM's sensitivity allows the retrieval of ripples and atom altitudes,[9] whilst its high-speed camera captures dynamic structures at millisecond intervals.[10] 4D-STEM technology measures ripples, partially addressing STEM's insensitivity to structures along the electron beam path.[5] While STEM records frames every few seconds,[11,12] HRTEM plays a crucial role in dynamic structure studies.[13–18] It is worth mentioning that HRTEM relies heavily on the microscope's performance. For direct atomic-scale imaging of TMD dynamics, a monochromator and extremely low aberrations are essential.[15–18]

Limited by the temporal coherence of the incident beam and distortions due to the aberration function, the interpretative resolution of HRTEM images often falls short of expectations. Temporal coherence directly attenuates high-frequency

[†]These authors contributed equally to this work.
[‡]Corresponding author. E-mail: chhjin@zju.edu.cn
[§]Corresponding author. E-mail: shglin@scau.edu.cn
[¶]Corresponding author. E-mail: linfang@scau.edu.cn

© 2025 Chinese Physical Society and IOP Publishing Ltd. All rights, including for text and data mining, AI training, and similar technologies, are reserved.

information, and an HRTEM image represents a superposition of images across a range of focal planes.[19] The distortion, primarily caused by the projection lens, complicates the direct interpretation of atomic information. For example, even if the atoms are aligned and their distances between columns exceed the resolution limit, the atomic columns may not appear as an ideal Gaussian intensity distribution.[20–23] Although the aberration parameters are directly given by *Cs*-corrected TEMs (aberration function and definitions in the SI methodology),[24,25] their accuracy is limited. This makes it difficult to simulate an HRTEM image that exactly matches the experimental image, even for simple structures like graphene.[26]

Aberration parameters derived from amorphous HRTEM images may not be highly accurate when applied to crystalline specimens. Online measurement in *Cs*-corrected TEM involves recording the Zemlin tableau at a large defocus,[24,25,27,28] yielding the aberration parameters up to third order in standard mode and fifth order in advanced mode, respectively. However, researchers have to switch to a region of interest and set the Scherzer focus,[28] and the coil currents controlling the focus may affect other aberrations. Most offline methods focus on measuring low-order aberrations. For instance, the algorithm based on phase correlation functions[29–31] employs a pattern recognition procedure to measure the focus and 2-fold astigmatism,[32] fits Zernike polynomials to power spectra,[33] or averages the Thon ring to measure aberrations.[34,35] This is also because low-order aberrations, such as 2-fold astigmatism and axial coma, remain stable for only a short duration, typically lasting from a few minutes to half an hour.[36] Experiments suggest disparities between measured aberrations from amorphous specimens and their actual values, which also applies to aberrations measured from the online Zemlin tableau.[30]

Extracting aberration parameters from non-amorphous HRTEM images is a challenging task. Previously, an approach[37] utilizes the exit-wave function, reconstructed from a series of images at different focuses, alongside an expected image where each atom is represented by a Gaussian function tailored to its location. The aberration parameters are then determined iteratively. Though it requires a large-area image with dozens of lattice unit cells and accurate focuses for exit-wave reconstruction, it may be the only algorithm capable of calculating the astigmatism from the lattice.

If the aberrations can be eliminated directly in an experiment, for instance, in an HRTEM image of a monolayer, the atoms can be clearly identified.[15–18] However, most TEMs do not achieve such a level of excellence. Relying on the exit-wave reconstruction and measured aberrations, the lost but critical phase information can be recovered from the wave function at the specimen's exit surface using a series of focal images.[19,38–40] Also, deconvolution methods can be utilized to remove the effects of the contrast transfer function from HRTEM images.[41] Although it reconstructs the wave function with a high signal-to-noise ratio (SNR), it is unfortunate that only one wave function can be reconstructed with dynamic structure lost and the dynamic structure refers to the time-varying structures of the specimen, such as defect evolutionary. To our knowledge, very limited works have been reported on the exit-wave reconstruction for each image despite a poor SNR, such as the approaches that remove the asymmetrical aberrations from HRTEM images of graphene[22] and reconstruct the phase by assuming a constant amplitude.[26] A machine learning algorithm is employed for the reconstruction of a single HRTEM image.[42] However, since the machine-learning-based algorithm operates as a black box, it is difficult to quantitatively analyze the results between the reconstructed images and the original input images. A reconstruction strategy proposed recently has the ability to reconstruct the exit-wave function of each image in a focal series of HRTEM images with a higher SNR,[43] but it has not yet been validated on experimental images.

In this paper, a method to estimate the aberration parameters from two HRTEM images with different focuses is presented. The core idea is to identify the most similar simulated image in one large dataset to obtain the aberration values. Several images simulated at very different aberrations may be found to be quite similar to the experimental image, so another focal image is needed to confirm the optimal aberrations. The proposed method is validated by graphene simulations and applied to measure the aberration parameters with 25 variables of monolayer MoS_2 experimental images. The reconstruction algorithm[43] is used to reconstruct the exit-wave function to resolve the structural changes in defects, edges and ripples over time. Interestingly, these images may have been discarded previously due to the unexpected specimen holder movement in the experiments. However, this movement allows us to resolve the aberrations using the proposed algorithm.

2. Aberrations in HRTEM image

Aberrations are the most important factor distorting the HRTEM image and reducing its resolution. The aberration function introduced by the projection lens is added to the phase of the wave function at the exit surface of the specimen, distinctly affecting the high-frequency phase. The aberration function $\chi(u)$, generally described in the frequency space u, is defined by[24,25]

$$\chi(u) = \mathrm{Re}\left\{\frac{1}{2}f\lambda uu^* + \frac{1}{2}A_1\lambda u^{*2} + \frac{1}{3}A_2\lambda^2 u^{*3} + B_2\lambda^2 u^2 u^* + \frac{1}{4}Cs\lambda^3(uu^*)^2 + \frac{1}{4}A_3\lambda^3 u^{*4} + S_3\lambda^3 u^3 u^*\right.$$

$$+\frac{1}{5}A_4\lambda^4u^{*5}+D_4\lambda^4u^4u^*+B_4\lambda^4u^3u^{*2}$$
$$+\frac{1}{6}C_5\lambda^5(uu^*)^3+\frac{1}{6}A_5\lambda^5u^{*6}+\cdots\Big\}$$
$$=\mathrm{Re}\Big\{\frac{1}{2}f\lambda uu^*+\frac{1}{2}A_1\lambda u^{*2}+\chi'(u)\Big\}, \quad (1)$$

where λ is the wavelength of the incident electron and the frequency vector u^* is the conjugate of u in frequency space. In this equation, all other variables belong to aberrations: focus f, two-fold astigmatism A_1, spherical aberration Cs, three-fold astigmatism A_2, axial coma B_2, four-axis astigmatism A_3, star aberration S_3, five-fold astigmatism A_4, three-lobe aberration D_4, axial coma B_4, five-fold spherical aberration C_5, and six-fold astigmatism A_5. Specially, $\chi'(u)$ denotes the residual aberration function.

Additionally, the temporal and spatial coherence of the incident beam limits the resolution of the HRTEM image. In simulation theory, the simulated HRTEM image $I(r)$ in quasi-coherence is expressed as[19]

$$I(r)=\sum_{m=-M}^{M}\delta\varepsilon f_\Delta(m\delta\varepsilon)|\mathcal{F}^{-1}\{\varphi(u)T(u,f+m\delta\varepsilon)\}|^2, \quad (2)$$

where u is the frequency vector, $f_\Delta(m\delta\varepsilon)$ represents the proportion of the image at the focal $f+m\delta\varepsilon$, $\delta\varepsilon$ is the focal kernel determined by value M, the integer m ranges from $-M$ to M, and $T(u,f+m\delta\varepsilon)$ is the transfer function at the focal $f+m\delta\varepsilon$. The Δ is the parameter relating to the temporal coherence of the incident beam and the beam convergence angle α, which relates to the spatial coherence, is hidden in the transfer function $T(u,f)$, which is given by

$$T(u,f)=\exp[-\mathrm{i}2\pi\chi(u)]\exp\Big\{-\Big(\frac{\pi\alpha}{\lambda}\Big)^2[\nabla\chi(u)]^2\Big\}, \quad (3)$$

in which the term $\nabla\chi(u)$ is the gradient of the aberration function of Eq. (1) with λ being the wavelength of the incident wave.

3. Machine learning methods

In our scheme, five steps are required to measure the aberration parameters of HRTEM images, and the flowchart of this scheme is shown in Fig. 1(a). (i) Simulate HRTEM images: generate a large dataset of HRTEM images with randomized aberrations within a specific range, including some small rectangular images with their parameter list files. Each image is a snippet of a larger simulated image, equal in area to one motif, whose intensity at the upper left corner is maximized within this unit region. The intensity information, rather than the atomic position information, is used to snip the small regions due to the uncertainty in the atomic positions of the experimental images.

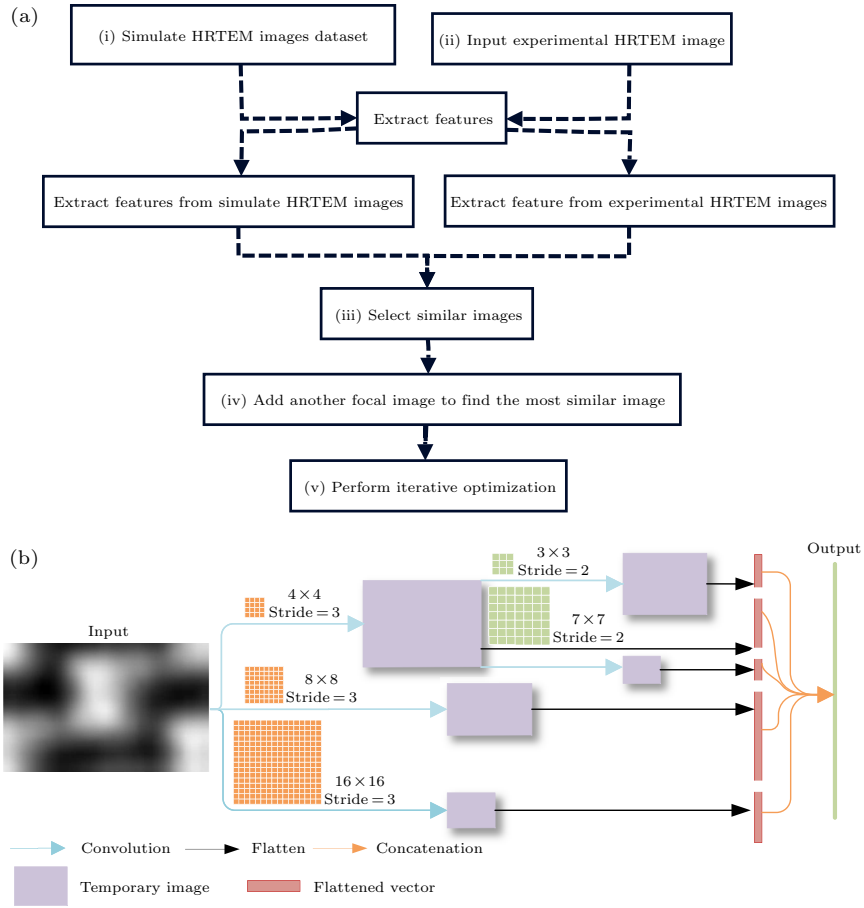


Fig. 1. (a) Flowchart for measuring the aberration parameters of HRTEM images. (b) The FEN-HRTEM for feature extraction from each small HRTEM image.

(ii) Feature extraction: a machine learning network shown in Fig. 1 is adopted to extract features from both the simulated and the experimental HRTEM images. (iii) Select similar images: identify the simulated images that are most similar to the experimental images by calculating the smallest Euclidean distances between the extracted feature vectors. (iv) Add another focal image: simulate images at various focal values using the aberration parameters of the selected images, determine the best match to the experimental image by comparing the Euclidean distances of features, and find the best aberrations. (v) Perform iterative optimization: change each aberration parameter independently to find the optimal values that best match the experimental image. Repeat the process with the additional simulated datasets or adjust the 4^{th} and 5^{th} steps if necessary.

The FEN-HRTEM (feature-extraction networks of HRTEM images) for feature extraction from small HRTEM images is illustrated in Fig. 1(b). The structure refers to the inception's architecture[44] and uses a multi-layer-multi-kernel structure: three central kernels of sizes 4×4, 8×8 and 16×16 pixels^2 with a convolution stride of 3 [denoted by the orange blocks in Fig. 1(b)] and two Gaussian kernels of sizes 3×3 and 7×7 pixel^2 with a convolution stride of 2 [denoted by the green blocks in Fig. 1(b)]. The central kernel emphasizes the mid-image shapes with a high center weight, while the small Gaussian kernels preserve the key features. All kernels are normalized. The purple blocks represent the intermediate images. The black arrows indicate the flattening operation. The final output is a concatenated feature vector. The Euclidean distance between these vectors indicates the most similar image compared to the experimental image, offering greater numerical variance than the traditional indices like image similarity, which can be efficiently computed in parallel.

4. Algorithm tested by simulation images

A graphene sample is used to validate the algorithm with eight parameters yet to be determined. A total of 500000 simulated images are generated using the ToTEM software.[45] The imaging conditions are 80 kV acceleration voltage, 2.0 nm focal spread, 0.2 mrad beam convergence angle, and ranges for focus (-2.5 ± 4.0 nm), A_1 (2.5 ± 2.5 nm), A_2 (40.0 ± 10.0 nm), B_2 (35.0 ± 10.0 μm), and Cs (4.0 ± 1.0 μm). The astigmatism angles range from 0° to 180°. The variables are uniformly distributed within their intervals. The test images excluded from the dataset are simulated. As another focal image is required for confirming the aberrations, the image with a changed focal length needs to be simulated, where all parameters are the same as those of the test image, but the focus value is increased by +1.0 nm. Figures 2(a) and 2(b) show a test image and its focal image, respectively.

The FEN-HRTEM method is used to extract features from the test image in Fig. 2(a), as well as all the images in the dataset. The Euclidean distances between the images in dataset and the test image are then calculated to identify the best matches. The four most similar images, labeled as #1 to #4, are depicted in Fig. 2(c) with the corresponding Euclidean distances of 8.82, 10.61, 11.04, and 11.05. Based on the aberration values of these four images, other four images are simulated with their focuses increased by +1.0 nm, as shown in Fig. 2(d). Calculating the Euclidean distances between Figs. 2(d) and 2(b) yields the values of 82.25, 21.09, 24.63, and 45.32 for images #1 to #4, respectively. Such results indicate that the rank from best to worst match is #2, #3, #4, and #1. This is corroborated by the radar chart in Fig. 2(e), where the red dotted, green solid, black solid, and purple dotted lines represent the parameters of images #1 to #4, respectively, while the yellow area indicates the true parameter values of Fig. 2(a).

Further optimization in the 5^{th} step of the proposed scheme improves accuracy. As shown in the radar map in Fig. 2(f), the aberration parameters after optimization for #2 and #3 and represented by the dashed lines are closer to the yellow region than the solid lines, indicating that the optimized aberrations are closer to the expected values, which are represented by the yellow region. To illustrate the optimization process, using image #2 as an example, Fig. 2(g) shows the Euclidean distances of the features for some variables. These distances are determined by comparing the feature of Fig. 2(a) with those of images simulated by varying a single variable within a 20% focal range, while keeping other variables fixed at image #2's values. For instance, the focus is optimized within $-4.59\pm8.0\times20\%$ nm, where -4.59 nm is image #2's focus and 8.0 nm is the focal search range. After optimization, the focus and the magnitudes of A_1 and A_2 become -4.59, 2.05, and 48.0 nm, respectively. The azimuth angle of A_1 reaches its best value.

To verify the accuracy improvement, the aberrations are measured for 1000 HRTEM images in the test set. An accuracy ratio is defined as the absolute difference between the measured and true values divided by the search range. Figure 2(h) displays the averaged parameter differences for each parameter over 1000 images. Three scenarios are presented: (i) the parameters from the images with the minimum Euclidean distance in the dataset; (ii) the parameters confirmed by their focal-changed images; and (iii) further separately optimized parameters. These scenarios correspond to steps three, four, and five in the scheme, which are represented by the green, orange, and purple bars in Fig. 2(h), respectively. Importantly, the accuracy of the parameters has been improved, although different parameters have been improved to different extents with different error uncertainties after measurement,

which depends on how the parameters affect the image. The accuracy of the B_2 amplitude is the lowest due to its primary effect on image pattern shifts. Additionally, the accuracy of A_2 is relatively poor because A_2 corresponds to the third-order symmetry, which aligns with graphene's inherent third-order symmetry.

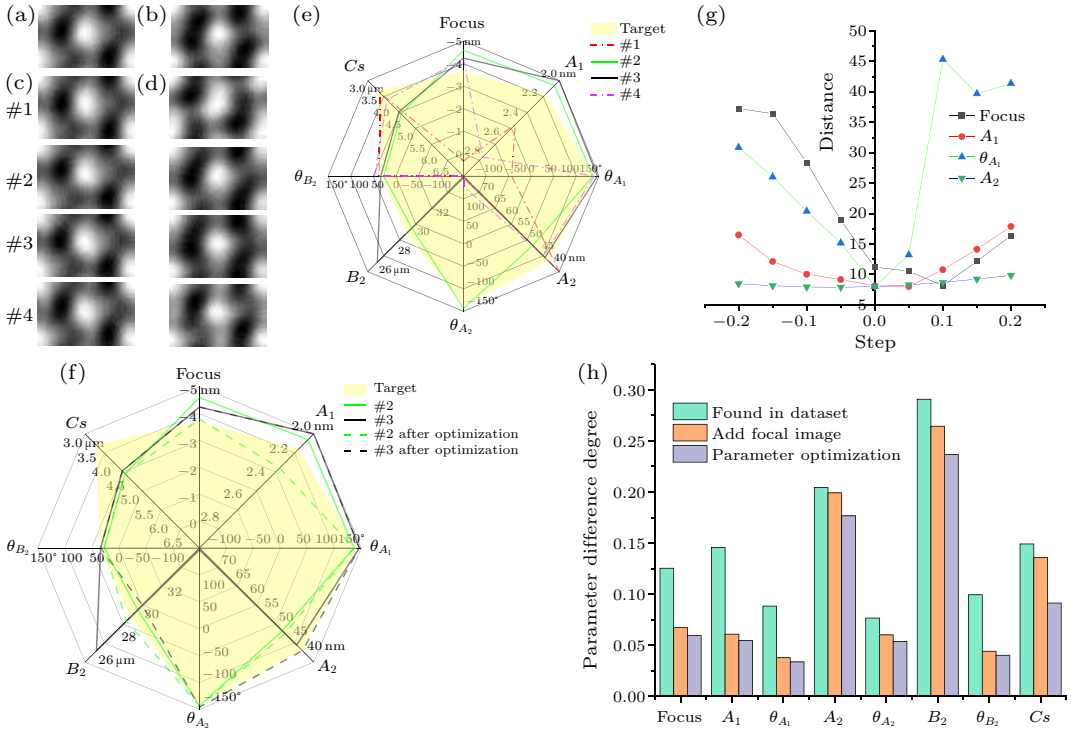


Fig. 2. (a) The test image and (b) another focal image. The focus value of (b) is +1.0 nm greater than that of (a). (c) Four images with the minimum Euclidean distance compared to (a) found in a dataset. (d) The focal images of (c). The focus values of (d) are +1.0 nm greater than those of (c). (e), (f) Radar diagrams of the aberration parameters. The target refers to the parameters of (a). The red, green, black and magenta lines in (e) denote the parameters from #1 to #4, respectively. The green and black lines in (f) represent the parameters of #2 and #3 before and after applying optimizations, respectively. (g) Euclidean distances related to focus, A_1 amplitude with varying azimuth angle, and A_2 amplitude. (h) Averaged parameter difference degree for 1000 test images. Green, orange, and purple bars represent the images found in the dataset, confirmed by another focal image, and applied optimization, respectively.

5. Application to the experimental images

5.1. Aberration measurements

The scheme is applied to the experimental HRTEM images of MoS_2 captured at 80 kV in a *Cs*-corrected TEM without a monochromator at an interval of one second between frames. Figures 3(a) and 3(b) show the first and fifth raw images, with the red-rectangle areas enlarged for details. To obtain a clear periodic motif (containing three Mo and three disulfide atoms, referring to one group of atoms), multiple motifs are averaged using the CalAtom software.[46] A small image, twice the area of a motif, is then cropped, as shown in the red rectangles in Figs. 3(c) and 3(d). The features in Figs. 3(c) and 3(d) are different due to a sudden movement of the sample holder, resulting in an obvious impact on focus. In Fig. 3(c), the black spots represent the atoms. However, the distances between the neighboring atoms are unequal, while the interior bright contrast pattern is distorted. In Fig. 3(d), the atomic positions in the hexagonal structure are indiscernible.

Due to limited performance of the computer, eight datasets with 500000 images each are generated based on the aberration parameter ranges listed in Fig. 3(e), which are primarily set according to the experimental parameters and confidence values (Figs. S1 and S2). All asymmetric aberration azimuth angles span from $-180°$ to $180°$. There are 25 parameters composing a vast high-dimensional parameter space.

The proposed scheme is applied to extract the features of each image, a total of 4000000 images. By calculating the Euclidean distances between the features of the images in the dataset and those of the experimental image highlighted in the red box in Fig. 3(d), the six images most similar to the experimental image, which exhibit the smallest distances, are displayed in Fig. 3(f) and labeled from #1 to #6. Their respective Euclidean distances are 17.26, 21.16, 25.54, 23.96, 28.28, and 23.09. Using the aberration parameters derived from each image in Fig. 3(f), the aberrations are further refined to produce improved simulated images that are even more similar to the experimental image, as shown in Fig. 3(g). The Euclidean distances for the images in Fig. 3(g) are 16.22, 19.71, 16.49, 18.22, 24.83, and 18.81, respectively. These values indicate greater similarity to the image in red box of Fig. 3(d) after refinement. The residual aberration functions plotted from these parameters, as defined in Eq. (1), are shown in Fig. 3(h), in which a flat region of about 24.0 mrad is indicated by blue

lines, corresponding to a resolution of approximately 1.75 Å.

Due to the unknown movement of the specimen holder along the electron beam, Fig. 3(i) closely resembles the image in red box of Fig. 3(c) the most among a series of HRTEM focal images with all the rest parameters known from Fig. 3(g). This allows the determination of the focal values for Fig. 4(c). Quantitatively, the Euclidean distances between the image sets in Fig. 3(i) and the image in red box of Fig. 3(c) are 55.38, 38.50, 52.90, 41.96, 48.87, and 36.54, respectively, from which one may conclude that image #6 is the closest match (aberrations listed in SI Tables S1 and S2). Also, the focuses of Figs. 3(c) and 3(d) are obtained as −16.72 nm and −12.56 nm, respectively.

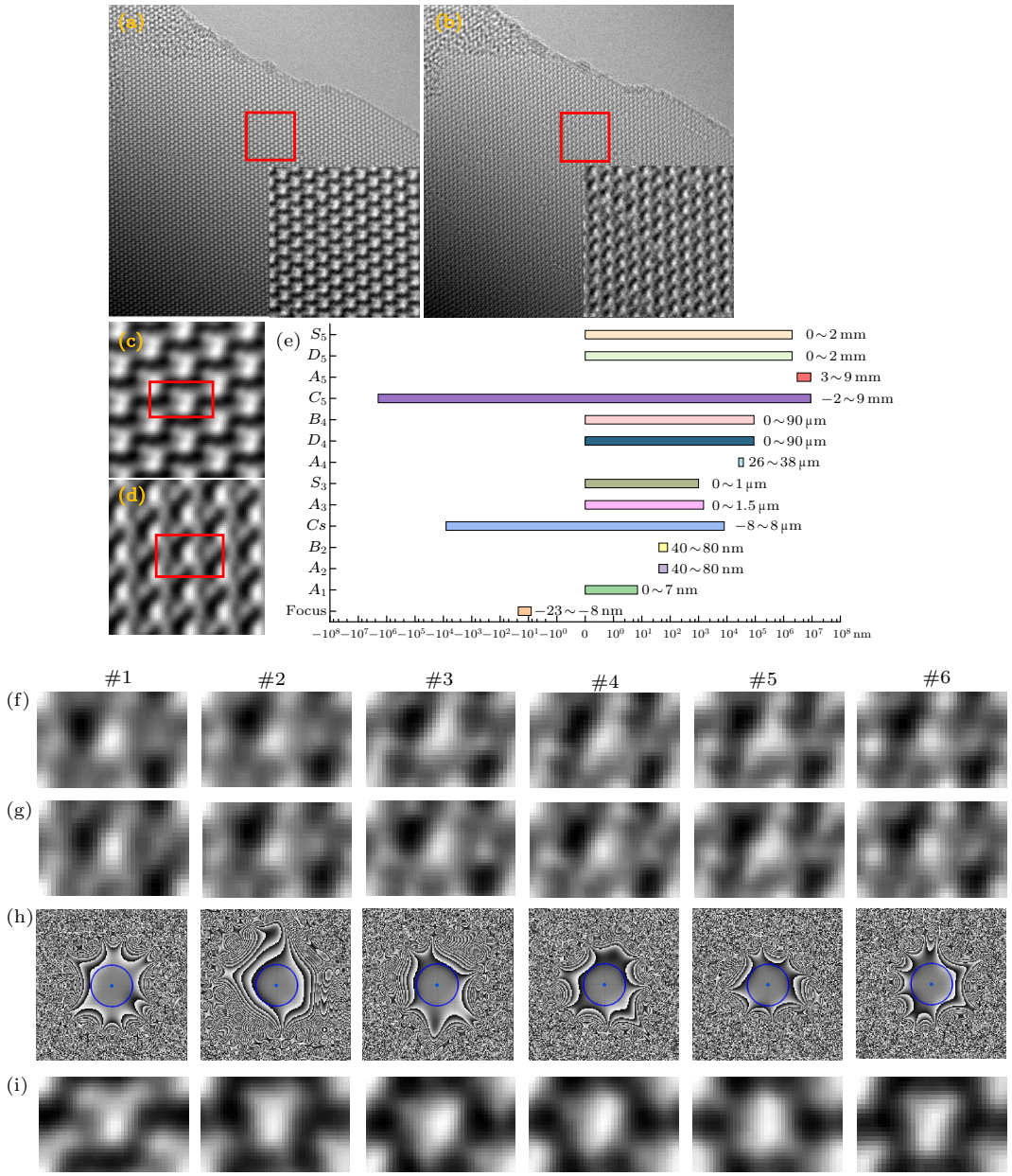


Fig. 3. (a) The 1st and (b) the 3rd experimental HRTEM images of monolayer MoS_2, with enlarged red-box regions in the lower right corners. (c) and (d) Averaged local regions from several periodic motifs for (a) and (b), with red-box regions intercepted for matching. (e) Amplitude ranges of all aberrations in the dataset. (f) Images directly found from the datasets. (g) Simulated images with the parameters optimized from (f). (h) Residual aberration functions for images in (f); blue circles' radius: 24 mrad. (i) Focal images most similar to (c), simulated using the parameters from (f).

5.2. Phase retrieval and structure analyses

Based on the known aberration parameters, the exit-wave function is reconstructed for each HRTEM image (details in the SI methodology).[43] The exit-wave phases, influenced either by or free from the residual aberration function, show distinct differences (see Figs. S3 and S4). From the phase of the reconstructed exit-wave function, the structural evolution becomes evident.

First, the S-vacancy point defects exhibit positional variations. Figure 4(a) depicts a region extracted from the first

three raw images (details in Fig. S5), while Fig. 4(b) presents the phases derived from the reconstructed exit-wave function. The small arrows in Fig. 4(b) indicate the locations where a single sulfur atom is absent. The contrast of these point defects is notably lower compared to the rest of the atoms and they vary in positions (additional images can be viewed in Fig. S6). Notably, atoms appear brighter in the phase images, whereas darker spots in the raw images represent the atoms, and the raw images lack sufficient clarity to resolve the structure.

Second, the amorphous structures at the edges and the line defects on the monolayer MoS_2 are more clearly visible than in the raw images. The structure evolution at the vacuum edge is depicted in Figs. 4(c) and 4(d). The complex atomic structure, resembling an amorphous state, appears to be resolved. Such structures cannot be accurately estimated through theoretical calculations. Instead, the clustering and dynamic movement of Mo-rich structures close to the vacuum edge are more intuitively revealed. An additional example, featuring the transition from a step to a flatter edge, is illustrated in Fig. S7.

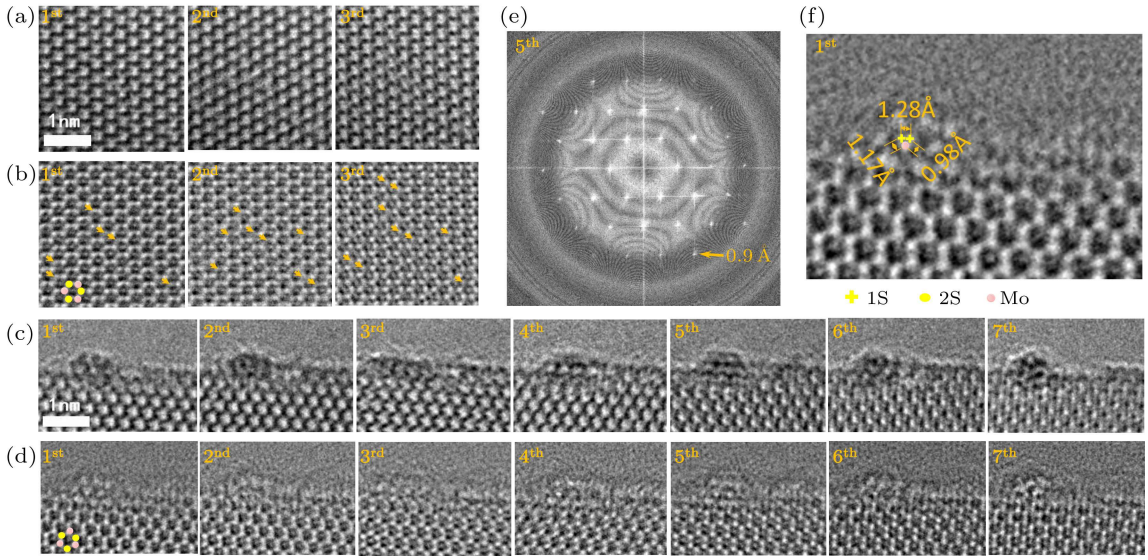


Fig. 4. (a), (c) The experimental images and (b), (d) their reconstructed phases, showing (a), (b) the point defects and (c), (d) the structural evolution close to the vacuum edge. The orange arrows indicate single sulfur atom vacancies. The yellow and pink spots denote the disulfide and Mo atoms, respectively. (e) The power spectrum of the phase of the exit-wave function reconstructed from the 5th image. The resolution of 0.9 Å is indicated by an orange arrow. (f) The magnified phase of the 1st image in (d), showing the single Mo and S atoms and their on-plane distances. The Mo atom, single S-vacancy and disulfide atoms are represented by pink dot, yellow plus signs and yellow dots, respectively. The distances between three neighbor sites are marked. The number in the top left corner identifies the frames extracted from the time-series image stack at the same location.

The clear evolution at the edge benefits from the improved resolution, which is approximately 0.9 Å. Figure 4(e) shows the power spectrum of the phase image of the exit-wave function reconstructed from the 5th image, where the imaginary part of the modulation transfer function can be seen, whereas there is no such evidence in the power spectrum of the reconstructed exit-wave function (more power spectra in Fig. S8). The resolution of approximately 0.9 Å is evident in Fig. 4(e) and holds true for every reconstructed wave. Figure 4(f) shows three atoms close to each other and their distances, which is the magnified phase of the 1st image in Fig. 4(d); these atoms can be identified as single Mo and S atoms according to their intensity, represented by a purple dot and two yellow plus signs. Specially, the distances between very close atomic sites have been measured as 1.28 Å, 1.17 Å and 0.98 Å in Fig. 4(f).

Third, the direct solution of structural evolution with multiple missing atoms is demonstrated. Figures 5(a) and 5(b) depict this process applied on the HRTEM images and the reconstructed phase, respectively. Specifically, the phase images in Fig. 5(b) are enhanced with a brightness of 38 and a contrast of 82 to highlight the atomic information (these values are adjusted based on visual perception and readers can find the raw phases in Fig. S9 for better comparison), with the atoms indicated by dots to illustrate the evolution. Initially, the 3rd image shows only a few S vacancies. Subsequently, more atoms, including Mo atoms, are progressively missing from the 4th to the 6th images.

Also, the evolution of the S-vacancy line defect is shown in Figs. 5(c) and 5(d), displaying the raw images and the phase of the exit-wave function, respectively. The phase images have the same brightness and contrast as those in Fig. 5(b) (raw phases in Fig. S10). The line defect, marked by a red cross, becomes longer in the 4th and 5th images and then disappears from the 6th to the 7th image. In the 7th image, the Mo atoms, indicated in pink in Fig. 5(d), form a different structure nearly adjacent to the vacuum. This structure consists of about four parallel S-vacancy lines.[18] At the edge, a small region with two layers of MoS_2 in an AA stacking configuration may emerge. It is identified by a higher atomic contrast and indicated by a blue arrow in Fig. 5(d).

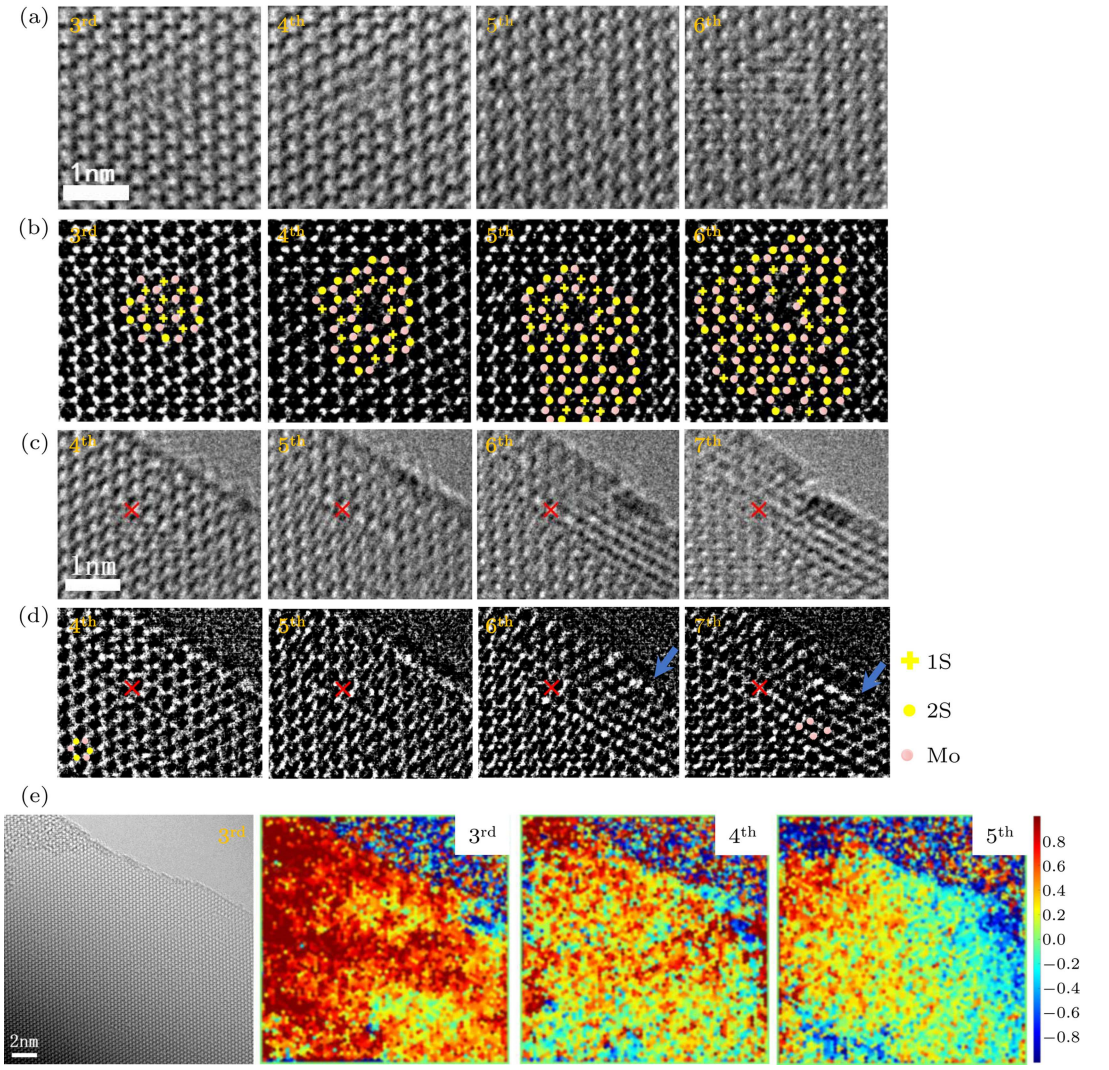


Fig. 5. (a)–(d) The evolution of the missing atoms and the S-vacancy line defects. (a), (c) The experimental images and (b), (d) their enhanced-contrast reconstructed phases, showing (a), (b) the missing atoms and (c), (d) the S-vacancy line defects. The orange arrows mark single sulfur atom vacancies. The yellow and pink spots denote the disulfide and Mo atoms, respectively. The yellow cross denotes the single S atom. In (c), (d), the red crosses label the same positions and the blue arrows indicate the structure containing two layers. (e) The gray image is the 3rd experimental image and the colorful images are the ripple morphology from the 3rd to the 5th experimental images. Colorbar units: nanometers.

Last, the ripple of the monolayer MoS_2 may be measured from the reconstructed exit-wave function. This is possible because the exit-wave function propagates along the electron incident direction via computation. The best-focusing condition for each small region, containing a group of atoms, corresponds to the ripple altitude of the monolayer MoS_2. Under the optimal focus, the image has the best clarity and is the closest to the ideal one. Figure 5(e) shows the 3rd experimental image and the ripple morphology of the 3rd, 4th and 5th images. The ripple morphology primarily represents height differences, with a reference plane perpendicular to the direction of the electron beam incidence. The color confusion in the upper right corner is due to the vacuum, and the ripple of the monolayer MoS_2 agrees with the expected ripple behavior of a free-standing monolayer in TEM.

6. Conclusions

Due to the imprecision in measuring aberrations and the challenge of eliminating the aberration function in *Cs*-corrected TEM, there is room for improving the resolution of HRTEM images via numerical algorithm. To remove the influence of lens aberrations, aberration parameters must be determined precisely first.

From lattice images of small regions, a machine learning-based algorithm is proposed to find the image most similar to the experimental image from a large number of simulated images, thereby determining the aberrations in the experimental images. Although the database needs to be regenerated for different crystal structures, the range of aberration parameters is large due to the parameter optimization step. For images from other experiments with similar conditions on the same structure, it is not necessary to regenerate the image dataset again. Even in our case, focal images are recorded due to the

unexpected movement of the specimen holder and when the precision of the aberrations or the condition of the electron microscope is below expectations. For the experimental images of monolayer MoS_2, we identified the values of 25 variables, which are 14 aberrations in total. Based on these parameters, the phases of the exit-wave function could be reconstructed with a resolution improved from about 1.75 Å to 0.90 Å for each image in a focal series. This allowed us to get the atomic structure and the ripple morphology of monolayer materials, the evolution of S-vacancy point and line defects, and amorphous near edge become visible. These applications reveal the accuracy of the aberration measurement and its significance for further improvements in resolution.

Acknowledgement

F. Lin acknowledges financial support from the National Natural Science Foundation of China (Grant No. 61971201).

References

[1] Manzeli S, Ovchinnikov D, Pasquier D, Yazyev O V and Kis A 2017 *Nat. Rev. Mater.* **2** 17033
[2] Shanmugam V, Mensah R A, Babu K, Gawusu S, Chanda A, Tu Y, Neisiany R E, Försth M, Sas G and Das O 2022 *Part. Syst. Charact.* **39** 2200031
[3] Yang S J, Choi M Y and Kim C J 2023 *Adv. Mater.* **35** 2203425
[4] Rehman M U, Hua C Q and Lu Y H 2020 *Chin. Phys. B* **29** 057304
[5] Luo R, Gao M, Wang C, Zhu J, Guzman R and Zhou W 2024 *Adv. Funct. Mater.* **34** 2307625
[6] Zhao X, Fu D, Ding Z, Zhang Y, Wan D, Tan S J, Chen Z, Leng K, Dan J and Fu W 2018 *Nano Lett.* **18** 482
[7] Tai K L, Huang C W, Cai R F, Huang G M, Tseng Y T, Chen J and Wu W W 2020 *Small* **16** 1905516
[8] Mendes R G, Pang J, Bachmatiuk A, Ta H Q, Zhao L, Gemming T, Fu L, Liu Z and Rümmeli M H 2019 *ACS Nano* **13** 978
[9] Van Dyck D, Jinschek J R and Chen F R 2012 *Nature* **486** 243
[10] Chang S L, Dwyer C, Barthel J, Boothroyd C B and Dunin-Borkowski R E 2016 *Ultramicroscopy* **161** 90
[11] Lin Y, Dumcenco D O, Huang Y and Suenaga K 2014 *Nat. Nanotechnol.* **9** 391
[12] Robinson A W, Wells J, Moshtaghpour A, Nicholls D, Huang C, Velazco-Torrejon A, Nicotra G, Kirkland A I and Browning N D 2024 *Chin. Phys. B* **33** 116804
[13] Segawa Y, Yamazaki K, Yamasaki J and Gohara K 2021 *Nanoscale* **13** 5847
[14] Girit Ç O, Meyer J C, Erni R, Rossell M D, Kisielowski C, Yang L, Park C, Crommie M F, Cohen M L and Louie S G 2009 *Science* **323** 1705
[15] Warner J H, Lee G, He K, Robertson A W, Yoon E and Kirkland A I 2013 *ACS Nano* **7** 9860
[16] Li J, Hu C, Wu H, Liu Z, Cheng S, Zhang W, Shu H and Chang H 2016 *Cryst. Growth Des.* **16** 7094
[17] Robertson A W, Lee G, He K, Gong C, Chen Q, Yoon E, Kirkland A I and Warner J H 2015 *ACS Nano* **9** 11599
[18] Wang S, Lee G D, Lee S, Yoon E and Warner J H 2016 *ACS Nano* **10** 5419
[19] Coene W, Thust A, De Beeck M O and Van Dyck D 1996 *Ultramicroscopy* **64** 109
[20] Wang Z, Byun J, Lee S, Seo J, Park B, Kim J C, Jeong H Y, Bang J, Lee J and Oh S H 2022 *Nat. Commun.* **13** 5616
[21] Mohn M J, Biskupek J, Lee Z, Rose H and Kaiser U 2020 *Ultramicroscopy* **219** 113119
[22] Lehtinen O, Geiger D, Lee Z, Whitwick M B, Chen M, Kis A and Kaiser U 2015 *Ultramicroscopy* **151** 130
[23] Lin F, Jian J, Ye L and Jin C 2015 *Microscopy* **64** 311
[24] Uhlemann S and Haider M 1998 *Ultramicroscopy* **72** 109
[25] Zemlin F, Weiss K, Schiske P, Kunath W and Herrmann K 1978 *Ultramicroscopy* **3** 49
[26] Lin F, Ren X B, Zhou W P, Zhang L Y, Xiao Y, Zhang Q, Xu H T, Li H and Jin C H 2018 *Micron* **114** 23
[27] Zemlin J and Zemlin F 2002 *Ultramicroscopy* **93** 77
[28] Hetherington C 2004 *Mater. Today* **7** 50
[29] Meyer R R, Kirkland A I and Saxton W O 2002 *Ultramicroscopy* **92** 89
[30] Kirkland A I, Meyer R R and Chang L S 2006 *Microsc. Microanal.* **12** 461
[31] Kirkland A I and Meyer R R 2004 *Microsc. Microanal.* **10** 401
[32] Barthel J and Thust A 2010 *Ultramicroscopy* **111** 27
[33] Vargas J, Otón J, Marabini R, Jonic S, de La Rosa-Trevín J M, Carazo and Sorzano C 2013 *J. Struct. Biol.* **181** 136
[34] Vulović M, Franken E, Ravelli R B, van Vliet L J and Rieger B 2012 *Ultramicroscopy* **116** 115
[35] Huang Z, Baldwin P R, Mullapudi S and Penczek P A 2003 *J. Struct. Biol.* **144** 79
[36] Biskupek J, Hartel P, Haider M and Kaiser U 2012 *Ultramicroscopy* **116** 1
[37] Ophus C, Rasool H I, Linck M, Zettl A and Ciston J 2016 *Advanced Structural and Chemical Imaging* **2** 1
[38] Coene W, Janssen G, de Beeck M O and Van Dyck D 1992 *Phys. Rev. Lett.* **69** 3743
[39] Allen L J, Mcbride W, O'Leary N L and Oxley M P 2004 *Ultramicroscopy* **100** 91
[40] Hsieh W, Chen F, Kai J and Kirkland A I 2004 *Ultramicroscopy* **98** 99
[41] Wu K, Yang B S, Xue W H, Sun D P, Ge B H and Wang Y M 2024 *Chin. Phys. B* **33** 076802
[42] Larsen M H L, Dahl F, Hansen L P, Barton B, Kisielowski C, Helveg S, Winther O, Hansen T W and Schiøtz J 2023 *Ultramicroscopy* **243** 113641
[43] Zhang X, Chen S, Wang S, Huang Y, Jin C and Lin F 2024 *J. Microsc.* **296** 24
[44] Szegedy C, Liu W, Jia Y, Sermanet P, Reed S, Anguelov D, Erhan D, Vanhoucke V and Rabinovich A 2015 *Proceedings of the IEEE conference on computer vision and pattern recognition* p. 1
[45] Yuan P J, Wu K P, Chen S W, Zhang D L, Jin C H, Yao Y and Lin F 2022 *J. Microsc.* **287** 93
[46] Zhang Q, Zhang L Y, Jin C H, Wang Y M and Lin F 2019 *Ultramicroscopy* **202** 114